

Statics and Dynamics of Continuum Robots With General Tendon Routing and External Loading

D. Caleb Rucker, *Student Member, IEEE*, and Robert J. Webster, III, *Member, IEEE*

Abstract—Tendons are a widely used actuation strategy for continuum robots that enable forces and moments to be transmitted along the robot from base-mounted actuators. Most prior robots have used tendons routed in straight paths along the robot. However, routing tendons through general curved paths within the robot offers potential advantages in reshaping the workspace and enabling a single section of the robot to achieve a wider variety of desired shapes. In this paper, we provide a new model for the statics and dynamics of robots with general tendon routing paths that is derived by coupling the classical Cosserat-rod and Cosserat-string models. This model also accounts for general external loading conditions and includes traditional axially routed tendons as a special case. The advantage of the usage of this coupled model for straight-tendon robots is that it accounts for the distributed wrenches that tendons apply along the robot. We show that these are necessary to consider when the robot is subjected to out-of-plane external loads. Our experimental results demonstrate that the coupled model matches experimental tip positions with an error of 1.7% of the robot length, in a set of experiments that include both straight and nonstraight routing cases, with both point and distributed external loads.

Index Terms—Continuum robot, cosserat rod, flexible arms, tendon actuation.

I. INTRODUCTION

CONTINUUM robots offer a number of potential advantages over traditional rigid link robots in applications that involve reaching through complex trajectories in cluttered environments or where the robot must compliantly contact the environment along its length (see [2]–[5] for reviews). Because of inherent flexibility, the shape of a continuum robot may be affected by both actuation and external loading. Recent models that account for both have been derived for continuum robots with pneumatic actuation [6], [7], multiple flexible push-pull rods [8], [9], and a backbone that consists of concentric, pre-curved tubes [10].

In this paper, we derive such a model for continuum robots that are actuated by tendons. This widely employed class of

continuum robot utilizes an elastic structure (which we will refer to as the “backbone,” although it may be any elastic media) that is actuated by tendons that pass through hollow channels in the structure. Example elastic structures include a flexible tube with tendons in the walls [11] and an elastic rod with disks affixed along its length (e.g., [12] and [13], among others). The tendons are attached to the robot at various arc lengths, enabling base-mounted actuators to bend the robot by tensioning the tendons.

Characterization of robot shape using mechanics-based models has been the subject of much prior research. Early work by Chirikjian and Burdick [14]–[16] used continuum models to describe hyperredundant robots. Recent continuum robot modeling has focused on continuously flexible structures that are acted on by a variety of actuators or force/torque transmission mechanisms. For tendon-actuated robots, the consensus result is that when the tendons are tensioned, the backbone assumes a piecewise constant-curvature shape. This yields analytically simple kinematics and has been experimentally demonstrated on several different robots [5]. Li and Rahn [17] investigated this issue explicitly by using nonlinear elastica theory to determine bounds on the tendon support height and spacing such that a constant curvature approximation is valid for robots in the absence of external loading.

In addition to kinematic modeling, some results exist for describing the shape of tendon-actuated continuum robots that are under external loads. Gravagne *et al.* provide a comprehensive energy-based model for the statics and dynamics of a planar continuum robot with in-plane loads [12], [18], [19]. An early theoretical work toward elastica dynamics with embedded tendons is that of Davis and Hirschorn [20]. Cosserat rod theory has also recently shown promise as a general tool for describing the deformations of other (not tendon-based) continuum designs [6], [10]. Jones *et al.* [21] applied Cosserat theory to achieve real-time kinematics computations for tendon-actuated robots that are under external loads, based on modeling tendon actuation as a single point moment that is applied to the backbone where each tendon is attached.

In this paper, we extend previous work on the Cosserat rod-based approach by taking into account not only the attachment point moment, but also the attachment point force and the distributed wrench that the tendon applies along the length of the backbone. Our approach couples the classical Cosserat string and rod models to express these distributed tendon loads in terms of the rod’s kinematic variables. We illustrate the difference between this new coupled model and the point moment model for out of plane loads in Fig. 1 and provide an experimental comparison of the two in Section V.

Manuscript received September 10, 2010; revised March 4, 2011; accepted June 18, 2011. Date of publication July 18, 2011; date of current version December 8, 2011. This paper was recommended for publication by Associate Editor T. Murphey and Editor G. Oriolo upon evaluation of the reviewers’ comments. This work was supported in part by the National Science Foundation (NSF) under Award 0651803, and NSF CAREER Award IIS-1054331. A preliminary version of some portions of this paper was presented at the 2010 International Symposium of Experimental Robotics [1].

The authors are with Vanderbilt University, Nashville, TN 37235 USA (e-mail: daniel.c.rucker@vanderbilt.edu; robert.webster@vanderbilt.edu).

Color versions of one or more of the figures in this paper are available online at <http://ieeexplore.ieee.org>.

Digital Object Identifier 10.1109/TRO.2011.2160469

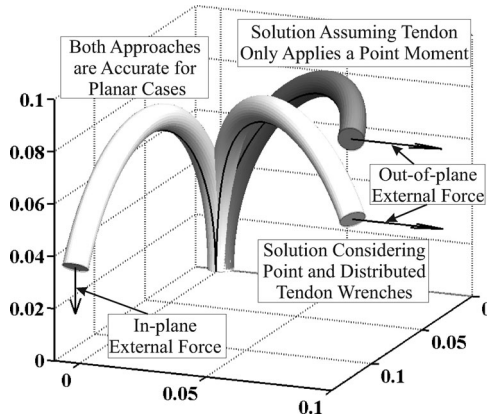


Fig. 1. Simulations of a continuum robot with a single, straight, tensioned tendon with in-plane and out-of-plane forces applied at the tip. These illustrate the difference between the model proposed in this paper that includes distributed tendon wrenches and the commonly used point moment approximation. For planar deformations and loads, the two models differ only by axial compression (which is small in most cases). However, for out-of-plane loads, the results differ significantly, and including distributed wrenches enhances model accuracy (see Section V).

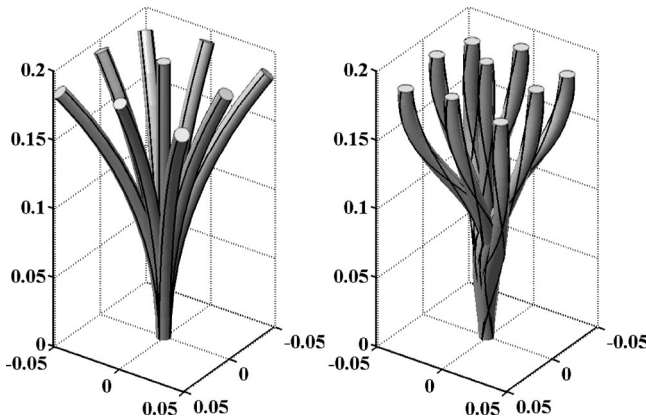


Fig. 2. Example of robot shape/workspace modification through the use of curved tendons. (Left) A robot with four straight tendons spaced at equal angles around its periphery. (Right) A similar robot with four helical tendons that each make one full revolution around the shaft. The two designs differ significantly in tip orientation capability, and the helical design may be better suited to, e.g., a planar industrial pick and place task.

A further advantage of the coupled approach is that it enables the use of tendon routing paths that are general curves in space (prior designs have routed tendons in straight paths along the robot, parallel to the backbone axis). This expands the design space and the set of shapes achievable for tendon-actuated robots. Fig. 2 illustrates how this can be useful for reshaping the workspace of a single-section robot, reorienting the gripper. This illustrative example could conceivably be valuable in industrial pick and place tasks where objects to be manipulated lie in a plane. Another example of the usefulness of general tendon routing is the cochlear implant of Simaan *et al.* [22], which uses a single curved tendon to control the shape of the implant during insertion, with the aim of reducing insertion forces and thereby trauma to the cochlea. Thus, enabling a single section of the robot to bend into variable curvature shapes may enhance the capabilities of continuum robots, and this can be achieved

by generally routed tendons. The model that we derive in this paper provides the theoretical framework for design and control of robots actuated in this way.

A. Contributions

In this paper, we provide a new model for the spatial deformation of tendon-actuated continuum robots. The model extends prior models by 1) treating tendon routing paths as general curves (relaxing the assumption of straight, axial routing), 2) accounting for the distributed wrenches that are applied by the tendon to the robot, which have been neglected by assumption in prior models, and 3) accounting for general external loads that are applied to the robot. Within this framework, we also describe the dynamics of the robot. Our experimental contributions include validation of the static model on a physical prototype. Some results in this paper were presented in preliminary form in [1]. Noteworthy additions/extensions include more extensive static experiments, the derivation and simulation of the dynamic model, and a quantitative experimental comparison of our new coupled model with the point-moment model.

II. CLASSICAL COSSERAT ROD MODEL

In this section, we provide a brief overview of the classical Cosserat rod model in order to familiarize the reader with the theory upon which our tendon-actuated continuum robot model is based. We follow some of the nomenclature and methods in Chapters 4 and 8 of Antman's thorough work on nonlinear elasticity [23], while making use of the kinematic notation familiar to roboticists (see [24]). The symbols used are summarized in a nomenclature section in the Appendix.

A. Rod Kinematics

In Cosserat-rod theory, a rod is characterized by its centerline curve in space $\mathbf{p}(s) \in \mathbb{R}^3$ and its material orientation, $R(s) \in \text{SO}(3)$ as functions of a reference parameter $s \in [0, \ell]$. Thus, a parameterized, homogeneous, rigid-body transformation, $g(s) \in \text{SE}(3)$, can be used to describe the entire rod:

$$g(s) = \begin{bmatrix} R(s) & \mathbf{p}(s) \\ 0 & 1 \end{bmatrix}.$$

Kinematic variables $\mathbf{v}(s)$ and $\mathbf{u}(s)$ represent the linear and angular rates of change of $g(s)$ with respect to s expressed in coordinates of the "body frame" $g(s)$. Thus, the evolution of $g(s)$ along s is defined by the following relationships:

$$\dot{R}(s) = R(s)\hat{\mathbf{u}}(s), \quad \dot{\mathbf{p}}(s) = R(s)\mathbf{v}(s) \quad (1)$$

where the dot denotes a derivative with respect to s , and the $\hat{\cdot}$ and \cdot^\vee operators are as defined in [24] (see also the Appendix).

We let the undeformed reference configuration of the rod be $g^*(s)$, where the z axis of $R^*(s)$ is chosen to be tangent to the curve $\mathbf{p}^*(s)$. One could use the Frenet-Serret or Bishop's convention to define the x and y axes of $R^*(s)$, or, if the rod has a cross section that is not radially symmetric, it is convenient to make the x and y axes align with the principal axes. The reference kinematic variables \mathbf{v}^* and \mathbf{u}^* can then be obtained

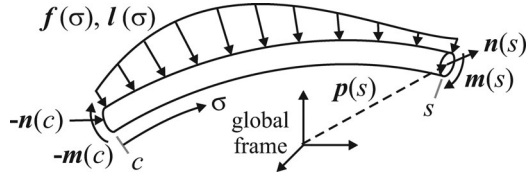


Fig. 3. Arbitrary section of rod from c to s subject to distributed forces and moments. The internal forces \mathbf{n} and moments \mathbf{m} are also shown.

by

$$[\mathbf{v}^{*T} \quad \mathbf{u}^{*T}]^T = (\mathbf{g}^{*-1}(s)\mathbf{g}^*(s))^\vee.$$

If the reference configuration happens to be a straight cylindrical rod with s as the arc length along it, then $\mathbf{v}^* = [0 \ 0 \ 1]^T$, and $\mathbf{u}^*(s) = [0 \ 0 \ 0]^T$.

B. Equilibrium Equations

Following [23], one can write the equations of static equilibrium for an arbitrary section of rod as shown in Fig. 3. The internal force and moment vectors (in global frame coordinates) are denoted by \mathbf{n} and \mathbf{m} , the applied force distribution per unit of s is \mathbf{f} , and the applied moment distribution per unit of s is \mathbf{l} . Taking the derivative of the static equilibrium conditions with respect to s , one arrives at the classical forms of the equilibrium differential equations for a special Cosserat rod:

$$\dot{\mathbf{n}}(s) + \mathbf{f}(s) = \mathbf{0} \quad (2)$$

$$\dot{\mathbf{m}}(s) + \dot{\mathbf{p}}(s) \times \mathbf{n}(s) + \mathbf{l}(s) = \mathbf{0}. \quad (3)$$

C. Constitutive Laws

The difference between the kinematic variables in the rod's reference state and those in the deformed state are related to various mechanical modes of strain. For instance, transverse shear in the body-frame x and y directions corresponds to $v_x - v_x^*$ and $v_y - v_y^*$, respectively, while axial elongation or stretch in the body-frame z direction corresponds to $v_z - v_z^*$. Similarly, bending about the local x and y axes are related to $u_x - u_x^*$ and $u_y - u_y^*$, respectively, while torsion about the local z axis is related to $u_z - u_z^*$.

One can use linear constitutive laws to map these variables to the internal forces and moments. With the assumption that the x and y axes of \mathbf{g}^* are aligned with the principal axes of the cross section, we have

$$\begin{aligned} \mathbf{n}(s) &= R(s)K_{se}(s)(\mathbf{v}(s) - \mathbf{v}^*(s)) \\ \mathbf{m}(s) &= R(s)K_{bt}(s)(\mathbf{u}(s) - \mathbf{u}^*(s)) \end{aligned} \quad (4)$$

where

$$\begin{aligned} K_{se}(s) &= \text{diag}(GA(s), GA(s), EA(s)), \quad \text{and} \\ K_{bt}(s) &= \text{diag}(EI_{xx}(s), EI_{yy}(s), EI_{zz}(s)). \end{aligned}$$

K_{se} is the stiffness matrix for shear and extension, and K_{bt} is the stiffness matrix for bending and torsion, where $A(s)$ is the area of the cross section, $E(s)$ is Young's modulus, $G(s)$ is the shear modulus, and $I_{xx}(s)$ and $I_{yy}(s)$ are the second moments

of area of the tube cross section about the principal axes. (Note that $I_{zz}(s) = I_{xx}(s) + I_{yy}(s)$ is the polar moment of inertia of the cross section about the z -axis pointing normal to the section and originating at its centroid.) We use these linear relationships here because they are notationally convenient and accurate for many continuum robots, but note that the Cosserat rod approach can also accommodate nonlinear constitutive laws.

D. Explicit Model Equations

We can now write (2) and (3) in terms of the kinematic variables using (4), their derivatives, and (1). By the assumption that the stiffness matrices are constant with respect to s , this leads to the full set of differential equations as follows.

$$\dot{\mathbf{p}} = R\mathbf{v}$$

$$\dot{R} = R\hat{\mathbf{u}}$$

$$\dot{\mathbf{v}} = \dot{\mathbf{v}}^* - K_{se}^{-1}(\hat{\mathbf{u}}K_{se}(\mathbf{v} - \mathbf{v}^*) + R^T\mathbf{f})$$

$$\dot{\mathbf{u}} = \dot{\mathbf{u}}^* - K_{bt}^{-1}(\hat{\mathbf{u}}K_{bt}(\mathbf{u} - \mathbf{u}^*) + \hat{\mathbf{v}}K_{se}(\mathbf{v} - \mathbf{v}^*) + R^T\mathbf{l}). \quad (5)$$

Alternatively, an equivalent system can be obtained by using \mathbf{m} and \mathbf{n} as state variables rather than \mathbf{v} and \mathbf{u} :

$$\dot{\mathbf{p}} = R\mathbf{v}, \quad \mathbf{v} = K_{se}^{-1}R^T\mathbf{n} + \mathbf{v}^*$$

$$\dot{R} = R\hat{\mathbf{u}}, \quad \mathbf{u} = K_{bt}^{-1}R^T\mathbf{m} + \mathbf{u}^*$$

$$\dot{\mathbf{n}} = -\mathbf{f}$$

$$\dot{\mathbf{m}} = -\dot{\mathbf{p}} \times \mathbf{n} - \mathbf{l}. \quad (6)$$

Boundary conditions for a rod which is clamped at $s = 0$ and subject to an applied force \mathbf{F}_ℓ and moment \mathbf{L}_ℓ at $s = \ell$ would be $R(0) = R_0$, $\mathbf{p}(0) = \mathbf{p}_0$, $\mathbf{m}(\ell) = \mathbf{L}_\ell$, and $\mathbf{n}(\ell) = \mathbf{F}_\ell$.

III. COUPLED COSSERAT ROD AND TENDON MODEL

Having reviewed the classical Cosserat-rod model, we now derive a new model for tendon-driven continuum manipulators. We use the Cosserat model of Section II to describe the elastic backbone, and we use the classic Cosserat model for extensible strings to describe the tendons. We will couple the string and rod models by deriving the distributed loads that the tendons apply to the backbone. These will be expressed in terms of the rod's kinematic variables and then incorporated into the rod model.

A. Assumptions

We employ two standard assumptions in our derivation. First, we assume frictionless interaction between the tendons and the channel through which they travel. This implies that the tension is constant along the length of the tendon. Frictional forces are expected to increase as the curvature of the robot increases due to larger normal forces, but the assumption of zero friction is valid if low friction materials are used, which is the case for most prior tendon-actuated continuum robots as well as our experimental prototype. Second, the locations of the tendons within the cross section of the robot are assumed not to change

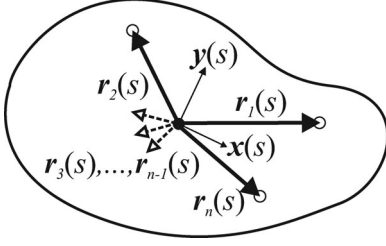


Fig. 4. General cross section of the continuum robot material or support disk, showing tendon locations.

during the deformation. This assumption is valid for designs which use embedded sleeves or channels with tight tolerances, as well as designs which use closely spaced standoff disks.

B. Tendon Kinematics

We separate the terms \mathbf{f} and \mathbf{l} in (5) into truly external distributed loads \mathbf{f}_e and \mathbf{l}_e and distributed loads due to tendon tension, \mathbf{f}_t and \mathbf{l}_t :

$$\begin{aligned}\mathbf{f} &= \mathbf{f}_e + \mathbf{f}_t \\ \mathbf{l} &= \mathbf{l}_e + \mathbf{l}_t.\end{aligned}\quad (7)$$

In order to derive \mathbf{f}_t and \mathbf{l}_t , we start by defining the path in which the tendon is routed along the robot length. Note that this path can be defined by channels or tubes within a homogeneous elastic structure or support disks on an elastic backbone, both of which afford considerable flexibility in choosing tendon routing. In our experimental prototype, we drill many holes around the periphery of each support disk, which allows easy reconfiguration of tendon path as desired.

A convenient way to mathematically describe the tendon routing path is to define the tendon location within the robot cross section as a function of the reference parameter s . Thus, we define the routing path of the i^{th} tendon by two functions $x_i(s)$ and $y_i(s)$ that give the body-frame coordinates of the tendon as it crosses the x - y plane of the attached backbone frame at s . As shown in Fig. 4, a vector from the origin of the attached frame to the tendon location is then given in attached frame coordinates by

$$\mathbf{r}_i(s) = [x_i(s) \quad y_i(s) \quad 0]^T. \quad (8)$$

The parametric space curve defining the tendon path in the global frame when the robot is in its undeformed reference configuration is then given by

$$\mathbf{p}_i^*(s) = \mathbf{R}^*(s)\mathbf{r}_i(s) + \mathbf{p}^*(s).$$

Similarly, when the robot is deformed due to tendon tension or external loads, the new tendon path in the global frame will be

$$\mathbf{p}_i(s) = \mathbf{R}(s)\mathbf{r}_i(s) + \mathbf{p}(s). \quad (9)$$

C. Distributed Forces on Tendons

The governing differential equations for an extensible string can be derived by taking the derivative of the static equilibrium

conditions for a finite section [23]. This results in the same equation for the internal force derivative as in (2):

$$\dot{\mathbf{n}}_i(s) + \mathbf{f}_i(s) = \mathbf{0} \quad (10)$$

where $\mathbf{f}_i(s)$ is the distributed force applied to the i^{th} tendon per unit of s , and $\mathbf{n}_i(s)$ is the internal force in the tendon. In contrast with a Cosserat rod, an ideal string has the defining constitutive property of being perfectly flexible, meaning it cannot support internal moments or shear forces but only tension [23], which we denote by τ_i . This requires that the internal force be always tangent to the curve $\mathbf{p}_i(s)$. Thus, we write

$$\mathbf{n}_i(s) = \tau_i \frac{\dot{\mathbf{p}}_i(s)}{\|\dot{\mathbf{p}}_i(s)\|}. \quad (11)$$

If friction were present τ_i would vary with s , but under the frictionless assumption, it is constant along the length of the tendon. Using (10) and (11) one can derive the following expression for the distributed force on the tendon (see the Appendix for derivation):

$$\mathbf{f}_i(s) = -\dot{\mathbf{n}}_i = \tau_i \frac{\hat{\mathbf{p}}_i^2}{\|\dot{\mathbf{p}}_i\|^3} \ddot{\mathbf{p}}_i. \quad (12)$$

D. Tendon Loads on Backbone

We can now write the collective distributed loads \mathbf{f}_t and \mathbf{l}_t that the tendons apply to the backbone, in terms of the individual forces on the tendons and their locations in the backbone cross section, as illustrated in Fig. 5. The total distributed force is equal and opposite to the sum of the individual force distributions on the tendons (12), namely

$$\mathbf{f}_t = -\sum_{i=1}^n \mathbf{f}_i.$$

The distributed moment at the backbone centroid is the sum of the cross products of each moment arm with each force. Thus

$$\mathbf{l}_t = -\sum_{i=1}^n (\mathbf{p}_i - \mathbf{p}) \times \mathbf{f}_i = -\sum_{i=1}^n (R\mathbf{r}_i) \wedge \mathbf{f}_i.$$

Substituting (12) yields

$$\begin{aligned}\mathbf{f}_t &= -\sum_{i=1}^n \tau_i \frac{\hat{\mathbf{p}}_i^2}{\|\dot{\mathbf{p}}_i\|^3} \ddot{\mathbf{p}}_i \\ \mathbf{l}_t &= -\sum_{i=1}^n \tau_i (R\mathbf{r}_i) \wedge \frac{\hat{\mathbf{p}}_i^2}{\|\dot{\mathbf{p}}_i\|^3} \ddot{\mathbf{p}}_i.\end{aligned}\quad (13)$$

We now express these total force and moment distributions in terms of the kinematic variables \mathbf{u} , \mathbf{v} , \mathbf{R} and \mathbf{p} so that we may substitute them into (7) and (5). To do this, we expand $\dot{\mathbf{p}}_i$ and $\ddot{\mathbf{p}}_i$. Differentiating (9) twice yields

$$\begin{aligned}\dot{\mathbf{p}}_i &= \mathbf{R}(\hat{\mathbf{u}}\mathbf{r}_i + \dot{\mathbf{r}}_i + \mathbf{v}) \\ \ddot{\mathbf{p}}_i &= \mathbf{R}(\hat{\mathbf{u}}(\hat{\mathbf{u}}\mathbf{r}_i + \dot{\mathbf{r}}_i + \mathbf{v}) + \hat{\mathbf{u}}\dot{\mathbf{r}}_i + \hat{\mathbf{u}}\ddot{\mathbf{r}}_i + \ddot{\mathbf{v}}).\end{aligned}\quad (14)$$

We here note that $\ddot{\mathbf{p}}$ is a function of $\dot{\mathbf{u}}$ and $\dot{\mathbf{v}}$. Therefore, if we substitute these results into (13) and then substitute (13) into

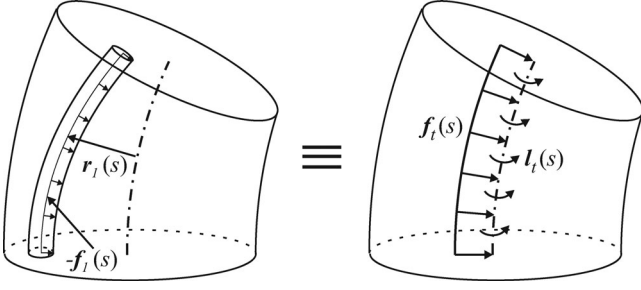


Fig. 5. A small section of rod that shows how the force distribution that the tendon applies to its surrounding medium is statically equivalent to a combination of force and moment distributions on the backbone itself.

the rod model (5) via (7), we obtain an implicitly defined set of differential equations. Fortunately, the resulting equations are linear in $\dot{\mathbf{u}}$ and $\dot{\mathbf{v}}$, and it is therefore possible to manipulate them into an explicit form. Rewriting them in this way (such that they are amenable to standard numerical methods) is the topic of the following section.

E. Explicit Model Equations

Our coupled rod and tendon model is given in implicit form by (5), (7), (13), and (14). In this section, we manipulate these implicit equations into explicit, first-order, state-vector form. To express the result concisely, we define some intermediate matrix and vector quantities, starting with (14) expressed in body-frame coordinates, i.e.,

$$\begin{aligned}\dot{\mathbf{p}}_i^b &= \hat{\mathbf{u}}\mathbf{r}_i + \dot{\mathbf{r}}_i + \mathbf{v} \\ \ddot{\mathbf{p}}_i^b &= \hat{\mathbf{u}}\dot{\mathbf{p}}_i^b + \hat{\mathbf{u}}\mathbf{r}_i + \hat{\mathbf{u}}\dot{\mathbf{r}}_i + \ddot{\mathbf{r}}_i + \dot{\mathbf{v}}.\end{aligned}$$

Now define vectors \mathbf{a}_i , \mathbf{a} , \mathbf{b}_i , and \mathbf{b} , as well as matrices A_i , A , B_i , B , G , and H as follows:

$$\begin{aligned}A_i &= -\tau_i \frac{(\hat{\mathbf{p}}_i^b)^2}{\|\hat{\mathbf{p}}_i^b\|^3}, & B_i &= \hat{\mathbf{r}}_i A_i \\ A &= \sum_{i=1}^n A_i, & B &= \sum_{i=1}^n B_i \\ G &= -\sum_{i=1}^n A_i \hat{\mathbf{r}}_i, & H &= -\sum_{i=1}^n B_i \hat{\mathbf{r}}_i \\ \mathbf{a}_i &= A_i (\hat{\mathbf{u}}\dot{\mathbf{p}}_i^b + \hat{\mathbf{u}}\mathbf{r}_i + \dot{\mathbf{r}}_i), & \mathbf{b}_i &= \hat{\mathbf{r}}_i \mathbf{a}_i \\ \mathbf{a} &= \sum_{i=1}^n \mathbf{a}_i, & \mathbf{b} &= \sum_{i=1}^n \mathbf{b}_i.\end{aligned}$$

We then find that \mathbf{f}_t and \mathbf{l}_t can be expressed as

$$\begin{aligned}\mathbf{f}_t &= R(\mathbf{a} + A\dot{\mathbf{v}} + G\dot{\mathbf{u}}) \\ \mathbf{l}_t &= R(\mathbf{b} + B\dot{\mathbf{v}} + H\dot{\mathbf{u}}).\end{aligned}\quad (15)$$

Substituting tendon load expressions into the last two equations of (5) and rearranging them, we have

$$(K_{se} + A)\dot{\mathbf{v}} + G\dot{\mathbf{u}} = \mathbf{d}$$

$$B\dot{\mathbf{v}} + (K_{bt} + H)\dot{\mathbf{u}} = \mathbf{c}$$

where the vectors \mathbf{c} and \mathbf{d} are functions of the state variables, as shown in the following:

$$\begin{aligned}\mathbf{c} &= K_{bt}\dot{\mathbf{u}}^* - \hat{\mathbf{u}}K_{bt}(\mathbf{u} - \mathbf{u}^*) \\ &\quad - \hat{\mathbf{v}}K_{se}(\mathbf{v} - \mathbf{v}^*) - R^T \mathbf{l}_e - \mathbf{b} \\ \mathbf{d} &= K_{se}\dot{\mathbf{v}}^* - \hat{\mathbf{u}}K_{se}(\mathbf{v} - \mathbf{v}^*) - R^T \mathbf{f}_e - \mathbf{a}.\end{aligned}$$

We can now easily write the governing equations as

$$\dot{\mathbf{p}} = R\mathbf{v}$$

$$\dot{R} = R\hat{\mathbf{u}}$$

$$\begin{bmatrix} \dot{\mathbf{v}} \\ \dot{\mathbf{u}} \end{bmatrix} = \begin{bmatrix} K_{se} + A & G \\ B & K_{bt} + H \end{bmatrix}^{-1} \begin{bmatrix} \mathbf{d} \\ \mathbf{c} \end{bmatrix}. \quad (16)$$

Noting that the quantities on the right-hand side of (16) are merely functions of the state variables and system inputs (\mathbf{u} , \mathbf{v} , R , τ_1, \dots, τ_n , \mathbf{f}_e and \mathbf{l}_e), we have arrived at a system of differential equations in standard explicit form that describes the shape of a continuum robot with any number of generally routed tendons and with general external loads applied.

This system can be solved by any standard numerical integration routine for systems of the form $\dot{\mathbf{y}} = \mathbf{f}(s, \mathbf{y})$. The required matrix inverse may be calculated (either numerically or by obtaining a closed form inverse) at every integration step, or one could alternatively rewrite the equations as a system with a state-dependent mass matrix on the left-hand side and use any standard numerical method for the solution of $M(\mathbf{y}, s)\dot{\mathbf{y}} = \mathbf{f}(s, \mathbf{y})$. For purposes of the simulations and experiments in this paper, we simply numerically invert.

F. Simplified No-Shear Model

It is often the case that the effect of shear and extension is negligible when computing the deformed shape of a rod. Below we give the explicit model equations which result from that assumption. Specifically, we let $\mathbf{v} = \mathbf{v}^* = [0 \ 0 \ 1]^T$. This results in the following:

$$\dot{\mathbf{p}} = R\mathbf{v}$$

$$\dot{R} = R\hat{\mathbf{u}}$$

$$\begin{aligned}\dot{\mathbf{u}} &= (H + K_{bt})^{-1} (K_{bt}\dot{\mathbf{u}}^* - \hat{\mathbf{u}}K_{bt}(\mathbf{u} - \mathbf{u}^*) \\ &\quad - \hat{\mathbf{v}}R^T \mathbf{n} - R^T \mathbf{l}_e - \mathbf{b})\end{aligned}$$

$$\dot{\mathbf{n}} = -R(\mathbf{a} + G\dot{\mathbf{u}}) - \mathbf{f}_e. \quad (17)$$

Note that (17) is provided for the reader's convenience. We use (16) for our experimental validation in Section V.

G. Boundary Conditions

When tendon i terminates at $s = \ell_i$ along the length of the robot, it applies a point force to its attachment point equal and opposite to the internal force in the tendon given by (11). Thus, the point force vector is given by

$$\mathbf{F}_i = -\mathbf{n}_i(\ell_i) = -\tau_i \frac{\dot{\mathbf{p}}_i(\ell_i)}{\|\dot{\mathbf{p}}_i(\ell_i)\|}. \quad (18)$$

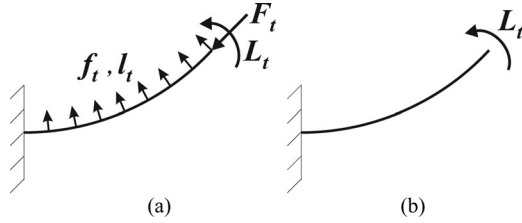


Fig. 6. (a) The coupled Cosserat rod and tendon approach includes all of the tendon loads. These loads are themselves functions of the robot shape, and therefore, the robot is treated as a coupled system. (b) The point moment approach only includes the attachment moment. For planar deformations, the two approaches predict similar robot shapes (see Fig. 1), but our experimental results in Section V show that for out-of-plane loading, the coupled approach is more accurate.

With a moment arm of $\mathbf{p}_i(\ell_i) - \mathbf{p}(\ell_i)$, this force creates a point moment \mathbf{L}_i at the backbone centroid of

$$\mathbf{L}_i = -\tau_i (R(\ell_i) \mathbf{r}_i(\ell_i)) \frac{\dot{\mathbf{p}}_i(\ell_i)}{\|\dot{\mathbf{p}}_i(\ell_i)\|}. \quad (19)$$

If at some location $s = \sigma$, point loads $\mathbf{F}(\sigma)$ and $\mathbf{L}(\sigma)$ (resulting from tendon terminations or external loads) are applied to the backbone, the internal force and moment change across the boundary $s = \sigma$ by

$$\begin{aligned} \mathbf{n}(\sigma^-) &= \mathbf{n}(\sigma^+) + \mathbf{F}(\sigma) \\ \mathbf{m}(\sigma^-) &= \mathbf{m}(\sigma^+) + \mathbf{L}(\sigma) \end{aligned} \quad (20)$$

where σ^- and σ^+ denote locations just before and just after $s = \sigma$. Any combination of external point loads and tendon termination loads can be accommodated in this way.

H. Point Moment Model

In prior tendon robot models, tendon actuation has often been modeled by the simple application of the pure point moment in (19) to an elastic backbone model at the location where each tendon is attached, without consideration of the point force at the attachment point and the distributed tendon loads along the length (see Fig. 6). This approach is convenient because it allows one to use the classical Cosserat rod (6) by the simple application of boundary conditions that take into account the tendon termination moments.

In [18], Gravagne justified this approximation for planar robots by showing that the effects of the point force and the distributed loads effectively “cancel” each other, leaving only the point moment. Thus, as shown in Fig. 1 this approach yields almost exactly the same final shape as the full coupled model when the robot deformation occurs in a plane.

However, as shown in Fig. 1, the two approaches diverge as the robot shape becomes increasingly nonplanar due to a transverse load at the tip. In Section V, we investigate the accuracy of both approaches through a set of experiments on a prototype robot.

IV. DYNAMIC MODEL

Based on the coupled rod and tendon model that was presented earlier for static continuum robot deformations, we now derive a model for the dynamics of a continuum robot with gen-

eral tendon routing. Such a model will be useful for the analysis of the characteristics of specific designs as well as the development of control algorithms that are similar to those derived for planar robots with straight tendons [12]. As we will show, addition of the necessary dynamic terms and compatibility equations results in a hyperbolic system of partial differential equations, which can be expressed in the standard form:

$$\mathbf{y}_t = \mathbf{f}(s, t, \mathbf{y}, \mathbf{y}_s) \quad (21)$$

where a subscript s or t is used in this section to denote partial derivatives with respect to the reference parameter s and time t , respectively.

We introduce two new vector variables, \mathbf{q} and $\boldsymbol{\omega}$, which are the body frame linear and angular velocity of the rod at s . These are analogous to \mathbf{u} and \mathbf{v} , respectively, but are defined with respect to time instead of arc length. Thus

$$\mathbf{p}_t = R\mathbf{q} \quad R_t = R\hat{\boldsymbol{\omega}}. \quad (22)$$

Recalling from (5) that

$$\mathbf{p}_s = R\mathbf{v} \quad R_s = R\hat{\mathbf{u}} \quad (23)$$

and using the fact that $\mathbf{p}_{st} = \mathbf{p}_{ts}$ and $R_{st} = R_{ts}$, we can derive the following compatibility equations:

$$\mathbf{u}_t = \boldsymbol{\omega}_s + \hat{\mathbf{u}}\boldsymbol{\omega}, \quad \mathbf{v}_t = \mathbf{q}_s + \hat{\mathbf{u}}\mathbf{q} - \hat{\boldsymbol{\omega}}\mathbf{v}. \quad (24)$$

Equations (2) and (3) describe the static equilibrium of the rod. To describe dynamics, we can add the time derivatives of the linear and angular momentum per unit length in place of the zero on the right-hand side, such that they become

$$\dot{\mathbf{n}} + \mathbf{f} = \rho A \mathbf{p}_{tt} \quad (25)$$

$$\dot{\mathbf{m}} + \dot{\mathbf{p}} \times \mathbf{n} + \mathbf{l} = \partial_t (R \rho J \boldsymbol{\omega}) \quad (26)$$

where ρ is the mass density of the rod, A is the cross-sectional area of the backbone, and J is the matrix of second area moments of the cross section. Expanding these and applying (24) one can obtain a complete system in the form of (21):

$$\begin{aligned} \mathbf{p}_t &= R\mathbf{q} \\ R_t &= R\hat{\boldsymbol{\omega}} \\ \mathbf{v}_t &= \mathbf{q}_s + \hat{\mathbf{u}}\mathbf{q} - \hat{\boldsymbol{\omega}}\mathbf{v} \\ \mathbf{u}_t &= \boldsymbol{\omega}_s + \hat{\mathbf{u}}\boldsymbol{\omega} \\ \mathbf{q}_t &= \frac{1}{\rho A} \left(K_{se} (\mathbf{v}_s - \mathbf{v}_s^*) + \hat{\mathbf{u}} K_{se} (\mathbf{v} - \mathbf{v}^*) \right. \\ &\quad \left. + R^T (\mathbf{f}_e + \mathbf{f}_t) - \rho A \hat{\boldsymbol{\omega}} \mathbf{q} \right) \\ \boldsymbol{\omega}_t &= (\rho J)^{-1} \left(K_{bt} (\mathbf{u}_s - \mathbf{u}_s^*) + \hat{\mathbf{u}} K_{bt} (\mathbf{u} - \mathbf{u}^*) \right. \\ &\quad \left. + \hat{\mathbf{v}} K_{se} (\mathbf{v} - \mathbf{v}^*) + R^T (\mathbf{l}_e + \mathbf{l}_t) - \hat{\boldsymbol{\omega}} \rho J \boldsymbol{\omega} \right) \end{aligned} \quad (27)$$

where \mathbf{f}_t and \mathbf{l}_t can be computed by using (15). Typically, conditions at $t = 0$ are given for all variables along the length of the robot, and the boundary conditions of Section III-G apply all the time.

TABLE I
TENDON ROUTING PATHS USED IN EXPERIMENTS

Tendon (i)	1	2	3	4	5	6
$x_i(s)$ (mm)	8	0	-8	0	$8 \cos(2\pi s/\ell)$	refer to (28)
$y_i(s)$ (mm)	0	8	0	-8	$8 \sin(2\pi s/\ell)$	refer to (28)

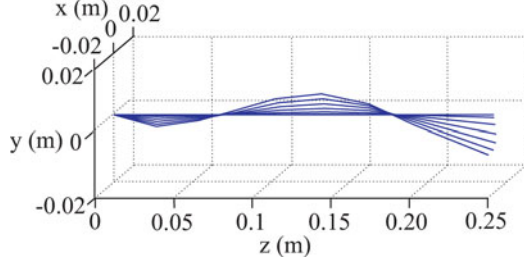


Fig. 7. The time response of a Continuum robot with a helical tendon is shown for a step input in tendon tension.

A. Dynamic Simulation

To illustrate the capability of (27) to describe the time evolution of the shape of a continuum robot with general tendon routing, we provide the following dynamic simulation of a robot whose backbone is identical to that of our experimental prototype in Section V. The robot contains a single tendon routed in a helical path where the tendon makes one complete revolution around the shaft as it passes from the base to the tip. This routing path is the same as the one for tendon 5 in our prototype, which is specified in Table I. Fig. 7 shows snapshots of the robot backbone shape at millisecond intervals after a step input of 5 N of tendon tension was applied. For the numerical algorithm, we used Richtmyer's two-step variant of the Lax–Wendroff finite-difference scheme implemented in a suite of MATLAB software written by Shampine [25].

The maximum length of the time step for any explicit time-marching algorithm for hyperbolic partial differential equations is limited by the Courant–Friedrichs–Lewy condition for stability. This is a fairly restrictive condition for dynamic rod problems because the shear, extension, and torsional vibrations are so fast that a very small time-step is required in order to capture them without the simulation becoming unstable. An active research field in mechanics and computer graphics simulation is to find reduced-order models of dynamic rods that are physically accurate, and yet capable of being simulated in real time (see, e.g., [26]). Future research for our coupled rod and string model will address computational efficiency, internal damping, and real-time dynamic control, but this simulation agrees with the intuition that the backbone should move toward a helical shape very quickly when the helical tendon undergoes a step input in tension.

V. EXPERIMENTAL VALIDATION

We now describe several different experiments conducted using a continuum robot prototype with a variety of tendon paths and external loading conditions.

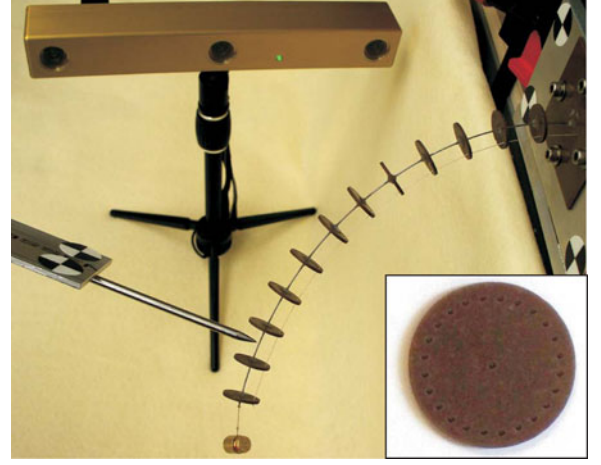


Fig. 8. In each experiment, a set of 3-D data points along the backbone was taken with an optically tracked stylus. (Inset) A standoff disk with a central hole for the backbone rod and outer holes through which tendons may be routed. Twelve copies of this disk were attached along the backbone, as shown in the larger image.

A. Prototype Construction

Our prototype robot is shown in Fig. 8. The central backbone is a spring steel rod (ASTM A228) of length $\ell = 242$ mm and diameter $d = 0.8$ mm with 12 stand-off disks, 20 mm in diameter, spaced 20 mm apart along its length. The disks were laser cut from a 1.57-mm-thick Teflon-filled Delrin plastic to minimize friction with the tendons. As shown in the inset of Fig. 8, 24 small pass-through holes were laser cut in a circular pattern at a radius of 8 mm from the center of each disk. The backbone rod was passed through the center holes of the disks, and each was fixed to it with Loctite 401. For tendons, we used 0.36-mm Teflon-coated fiberglass thread. Each tendon was run through various pass-through holes along the robot and knotted at the end, after passing through the final support disk. We note that in [17], the optimal ratio of tendon support spacing to offset distance from the backbone was found to be 0.4, and our prototype was designed to exactly match this ratio.

The tendon routing paths can be reconfigured on this robot by “rethreading” the tendons through a different set of holes in the various support disks. The robot's self-weight distribution was measured to be 0.47 N/m, which is enough to cause significant deformation, producing 44 mm of downward deflection at the tip (18% of the total arc length) for zero tendon tension. This weight was incorporated into all model calculations as a distributed force.

B. Experimental Procedure

In each of the following experiments, we applied known tensions to tendons behind the base of the robot by passing the tendons over low-friction pulleys and attaching them to hanging calibration weights. In those cases with applied point loads, we also hung weights from the tip of the robot.

In each experiment, a set of 3-D backbone points was collected by manually touching the backbone with the tip of an optically tracked stylus, as shown in Fig. 8. We used a

TABLE II
EXPERIMENTAL TENSIONS AND TIP LOADS

Experiments with Tendons 1 - 4 (Straight)							
Tension (N)	0	0.98	1.96	2.94	2.94	2.94	4.91
Tip Load (N)	0	0	0	0	0.098	0.196	0

Experiments with Tendon 5 (Helical)							
Tension (N)	0.98	1.96	2.94	4.91	4.91	4.91	6.87
Tip Load (N)	0	0	0	0	0.098	0.196	0

Experiments with Tendon 6 (Polynomial)					
Tension (N)	1.50	2.46	3.66	4.91	4.91
Tip Load (N)	0	0	0	0	0.0196

MicronTracker 2 H3-60 (Claron Technology, Inc.) to track the stylus, which has a specified fiducial measurement accuracy of 0.20 mm.

C. Calibration

The base frame position of the robot can be determined accurately with the optically tracked stylus. The angular orientation of the robot backbone as it leaves the base support plate is more challenging to measure. (Note that the backbone cannot be assumed to exit exactly normal to the plate due to the tolerance between the backbone and the hole drilled in the plate, and a 2° angular error in base frame corresponds to an approximately 8 mm tip error when the robot is straight.) The effective stiffness of the backbone was also increased due to the constraints of the standoff disks and Loctite adhesive at regular intervals. To account for these uncertainties, we calibrated the effective Young's modulus and the set of XYZ Euler angles (α , β , and γ) that describes the orientation of the base frame.

Our calibration process was accomplished by the solution of an unconstrained nonlinear optimization problem to find the set of parameters which minimizes the sum of the positional errors at the tip of the device for the set of 25 experiments with straight tendon paths described in Section V-D and Table II. In other words, for the parameter set $P = \{E, \alpha, \beta, \gamma\}$

$$P_{\text{cal}} = \operatorname{argmin}_P \left(\sum_{k=1}^{25} e_k \right)$$

where $e_k = \|\mathbf{p}_{\text{model}}(\ell) - \mathbf{p}_{\text{data}}(\ell)\|_k$ is the euclidean distance between the model tip prediction and the data in experiment k . To implement this minimization, we used the Nelder–Meade simplex algorithm, as implemented by MATLAB's `fminsearch` function.

To ensure fair comparison of the coupled model and the point moment model, the calibration procedure was performed separately for each model. Results are shown in Table III. Note that the similarity in calibrated Euler angles and their low deviation from nominal provides confidence that the correct base frame was obtained for both models. It is also important to note that the models contain the same number of parameters so that a fair comparison can be made. As expected, the calibrated values for Young's modulus are slightly higher than the nominal value of 210 GPa for spring steel, due to the increased stiffness provided by the disks and glue. Poisson's ratio was held constant

TABLE III
NOMINAL AND CALIBRATED PARAMETERS

Parameter	Nominal Value	Calibrated Value (Point Moment Model)	Calibrated Value (Coupled Model)
E (GPa)	210	227.9	229.6
α (deg)	180	177.7	177.9
β (deg)	0	2.2	2.2
γ (deg)	-90	-89.6	-89.7

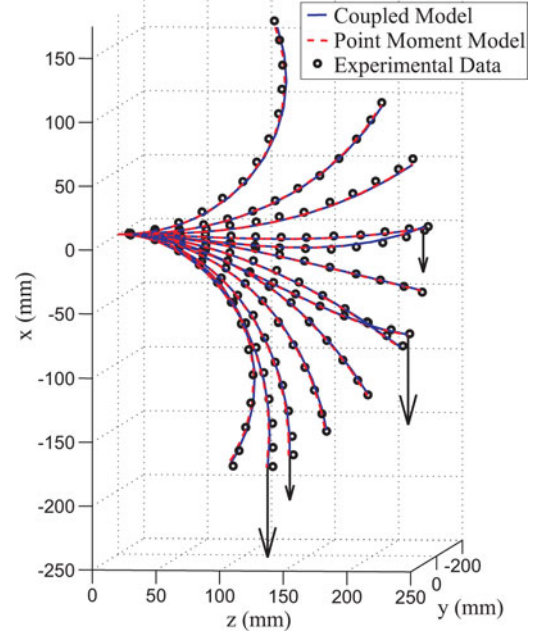


Fig. 9. Thirteen experimental cases with in-plane external loads. The tendons on the top and bottom of the robot (tendons 1 and 3) were tensioned and vertical tip loads were applied in four of the cases. Distributed gravitational loading is present in every case. As detailed in Table IV, both the coupled model and the point moment model are accurate and nearly identical for in-plane loads.

at $\nu = 0.3125$ during calibration so that the shear modulus was correctly scaled relative to Young's modulus.

D. Straight Tendon Results and Model Comparison

Table I details the location of the tendon routing paths used in our experiments in terms of $x_i(s)$ and $y_i(s)$, as defined in (8). We first performed 25 experiments (detailed in Table II) with straight tendon paths in order to compare the accuracy of the new coupled model with that of the point moment model. We detail the tip error statistics for both models with calibrated parameters in Table IV. The results for in-plane loading are accurate for both models, as shown in Fig. 9. In contrast, for out-of-plane loads, the coupled model provides more accurate predictions (see Fig. 10).

With calibrated parameters, the mean tip error over all 25 straight tendon experiments was 3.6 mm for the coupled model. This corresponds to 1.5% of the total arc length of the robot. Note that experimental data points lie close to the model prediction along the entire robot length, and the error increases gradually along the robot length so that tip error normalized by robot length is a reasonable metric for the accuracy of our model.

TABLE IV
MODEL TIP ERRORS FOR STRAIGHT TENDON EXPERIMENTS

13 Cases with In-Plane Loads				
Tip Error Statistic (mm)	mean	std. dev.	min	max
Point Moment Model	3.5	1.4	1.2	5.6
Coupled Model	3.1	1.3	0.3	5.3

12 Cases with Out-of-Plane Loads				
Tip Error Statistic (mm)	mean	std. dev.	min	max
Point Moment Model	9.8	5.5	1.7	16.2
Coupled Model	4.1	2.1	0.6	7.9

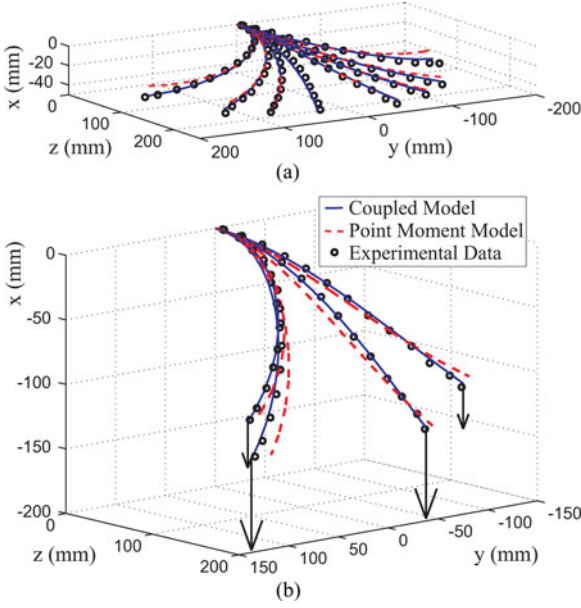


Fig. 10. Twelve experimental cases with out-of-plane external loads. The tendons on the left and right of the robot (tendons 2 and 4) were tensioned. (a) Distributed loading (robot self-weight) applied. (b) Additional tip loads applied. As detailed in Table IV, the data agrees with the coupled model prediction, but the point moment model becomes inaccurate as the out-of-plane load increases and as the curvature increases.

E. A High-Tension, Large-Load, Straight Tendon Experiment

We performed one additional straight tendon experiment to see how the two approaches compare for a case of large tension and large out-of-plane load, which is similar to the case simulated in Fig. 1. Tendon 4 was tensioned to 6.38 N and a downward tip force of 0.196 N was applied. The resulting data and model predictions are shown in Fig. 11. As illustrated in Fig. 1, the two models produce very different results, and we can now see from Fig. 11 that the coupled model prediction lies much closer to the data. Here, the tip error of the point moment model is 57 mm (23.5% of robot length), while the coupled model tip error is 12.8 mm (5.3% of robot length).

F. Experiments with Helical Tendon Routing

To explore more complex tendon routing, we experimentally evaluated helical routing paths. As given in Table I, our helical routing path winds through one complete revolution as it traverses the robot from base to tip. The tensions and tip loads for these experiments are detailed in Table II. Using the parameters calibrated from the previous straight tendon dataset, we plot the

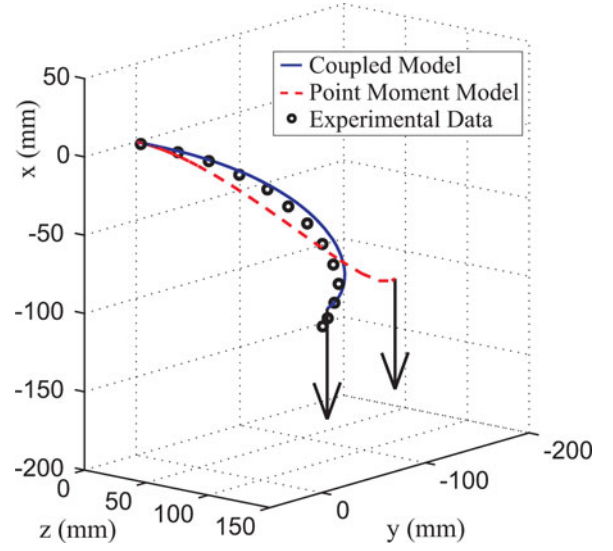


Fig. 11. Straight tendon case with high tension and high out-of-plane load, similar to the case depicted in Fig. 1. The data clearly indicate that the coupled model is more accurate than the point moment model.

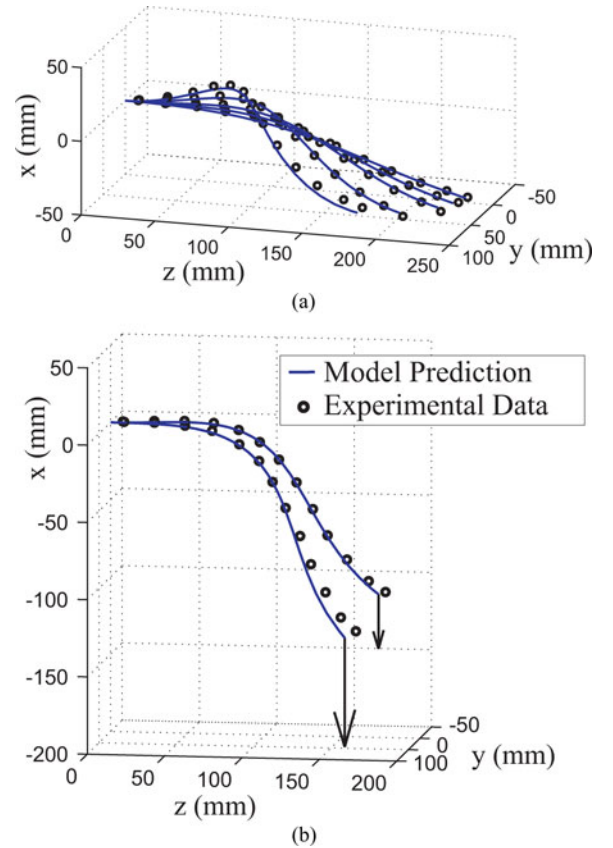


Fig. 12. Seven experiments performed with helical tendon routing (tendon number 5). (a) Self-weight only and (b) cases with external tip loads. Numerical tip errors are given in Table V (mean 5.5 mm).

resulting data and model predictions in Figs. 12 and 13. We see from Table V that the model agrees with the data with a mean tip error of 5.5 mm. The small increase in error over the straight tendon cases may be due to increased frictional forces, since the tension for the helical cases was higher.

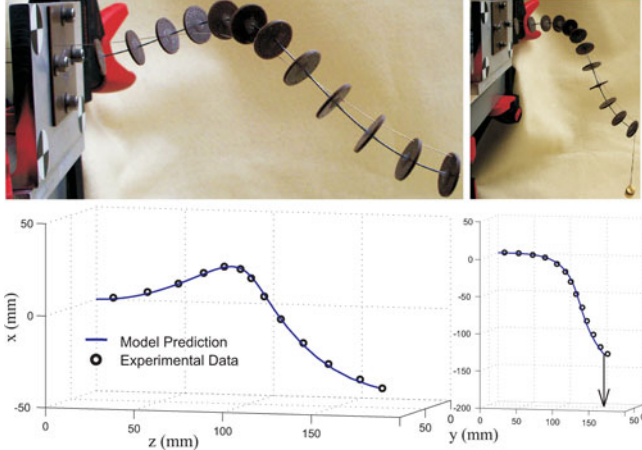


Fig. 13. Two helical cases are shown with photographs from the same angle for better visualization. (Left) The helical tendon is tensioned to 4.91 N, causing the backbone to assume an approximately helical shape which is deformed under its own weight. (Right) An additional 20-g mass hung from the tip causes large overall deflection.

TABLE V
MODEL TIP ERRORS FOR NONSTRAIGHT TENDON EXPERIMENTS

	mean	std. dev.	min	max
Tendon 5 (Helical)	5.5	2.7	1.9	10.0
Tendon 6 (Polynomial)	4.6	1.9	2.7	7.2

G. Experiments With Polynomial Tendon Routing

In order to further illustrate our model's generality, we performed additional experiments with a general curved tendon routing choice. We parameterized the routing path variables by two trigonometric functions whose arguments are defined by a fourth-degree polynomial function as follows:

$$\begin{aligned} x_6(s) &= 8 \cos(5887s^4 - 2849s^3 + 320s^2 + 6s) \\ y_6(s) &= 8 \sin(5887s^4 - 2849s^3 + 320s^2 + 6s) \end{aligned} \quad (28)$$

where s is in meters, and x_6 and y_6 are in millimeters. This routing path starts at the top of the robot, wraps around to the right-hand side for most of the length and then returns to the top at the end of the robot. The tensions and loads are given in Table II, and the results are detailed Table V and illustrated in Fig. 14. The coupled model's predictions agree with the data, with a mean tip error of 4.6 mm. This set of experiments confirms the coupled model's ability to handle arbitrary tendon routing choices.

H. Sources of Error

The largest source of measurement uncertainty is likely the procedure of manually placing the tip of the stylus on the robot during data capture. We estimate this uncertainty to be at most 2 mm. In general, the largest model errors occurred when the tendons were under the greatest tension. This agrees with the intuition that effects of static friction should become more significant as the tension and curvature increase. However, the low overall errors suggest that neglecting static friction is justifiable for this prototype.

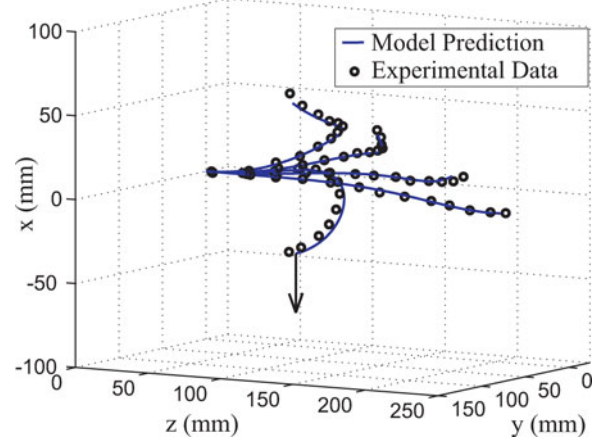


Fig. 14. Five cases with polynomial tendon routing as specified (28).

VI. CONCLUSION

In this paper, exact models for the forward kinematics, statics, and dynamics of continuum robots with general tendon routing, including external point and distributed loads has been derived. The models account for large deformations due to bending, torsion, shear, and elongation. The static model has been formulated as a set of nonlinear ordinary differential equations in state-vector form with boundary conditions, and the dynamic model consists of a system of hyperbolic partial differential equations.

Our experimental results demonstrated that this approach can accurately predict the shape of a physical prototype with both straight and nonstraight tendon routing paths and with external loading. With calibrated parameters, the mean tip error over all the experiments was 4.1 mm, or 1.7% of the total robot length. The straight tendon results also showed that the coupled model was twice as accurate as the point moment model for typical out-of-plane loading scenarios and far more accurate for a case with high tension and loading.

The models that have been developed in this paper can be useful as design tools, as well as provide the theoretical foundations for new control algorithms for tendon-actuated continuum robots. As illustrated in Fig. 2, the design space of achievable robot shapes can be expanded by the consideration of general tendon routing paths. We also believe that the models that are presented in this paper will pave the way for new quasi-static and/or dynamic control techniques for tendon-actuated continuum robots in the future. Furthermore, the inclusion of general external loads in tendon-actuated continuum robot models is an important step forward for future practical applications, given the robots' significant sag under self-weight and when carrying payloads. Future extensions of our model may address the issue of modeling static friction and real-time computation of the static and dynamic robot shape.

In summary, continuum robots have the potential to increase the performance of robotic systems that work in cluttered or unstructured environments, manipulating objects with the whole arm, or when compliant interaction with the environment is necessary. These capabilities appear useful in some traditional

industrial robotics applications, as well as in many new applications where traditional robots are not applicable due to lack of dexterity or danger of excessive force application. We believe that designs with general tendon routing and use of static and dynamic models accounting for external loading, such as those derived in this paper, will be key enablers of wider application of continuum robots in the future.

APPENDIX A

NOMENCLATURE

*	Variable in the reference state.
.	Derivative with respect to s .
$\widehat{}$	Converts \mathbb{R}^3 to $\mathfrak{so}(3)$ and \mathbb{R}^6 to $\mathfrak{se}(3)$:
$\widehat{\mathbf{u}} = \begin{bmatrix} 0 & -u_z & u_y \\ u_z & 0 & -u_x \\ -u_y & u_x & 0 \end{bmatrix}$ $\widehat{\begin{bmatrix} \mathbf{v} \\ \mathbf{u} \end{bmatrix}} = \begin{bmatrix} 0 & -u_z & u_y & v_x \\ u_z & 0 & -u_x & v_y \\ -u_y & u_x & 0 & v_z \\ 0 & 0 & 0 & 0 \end{bmatrix}.$	
∇	Inverse of the $\widehat{}$ operation. $(\widehat{\mathbf{u}})^\nabla = \mathbf{u}$.
s	$\in \mathbb{R}$ —Reference length parameter.
$\mathbf{p}(s)$	$\in \mathbb{R}^3$ —Position of the robot backbone centroid in global frame coordinates.
$R(s)$	$\in \text{SO}(3)$ —Orientation of the robot backbone material with respect to the global frame.
$g(s)$	$\in \text{SE}(3)$ —Homogeneous transformation containing $R(s)$ and $\mathbf{p}(s)$ (the “body frame”).
$\mathbf{r}_i(s)$	$\in \mathbb{R}^3$ —Position of the i^{th} tendon with respect to the body frame. $\mathbf{r}_i(s) = [x_i(s) \ y_i(s) \ 0]^T$.
$\mathbf{p}_i(s)$	$\in \mathbb{R}^3$ —Position of the i^{th} tendon in global frame coordinates. $\mathbf{p}_i(s) = R\mathbf{r}_i(s) + \mathbf{p}(s)$.
$\mathbf{u}(s)$	$\in \mathbb{R}^3$ —Angular rate of change of g with respect to s in body-frame coordinates. $\mathbf{u} = (R^T \dot{R})^\nabla$.
$\mathbf{v}(s)$	$\in \mathbb{R}^3$ —Linear rate of change of g with respect to s in body-frame coordinates. $\mathbf{v} = R^T \dot{\mathbf{p}}$.
$\mathbf{n}(s)$	$\in \mathbb{R}^3$ —Internal force in the backbone expressed in global frame coordinates.
$\mathbf{m}(s)$	$\in \mathbb{R}^3$ —Internal moment in the backbone expressed in global frame coordinates.
$\mathbf{f}_e(s)$	$\in \mathbb{R}^3$ —External force per unit s on the backbone in global frame coordinates.
$\mathbf{l}_e(s)$	$\in \mathbb{R}^3$ —External moment per unit s on the backbone in global frame coordinates.
$\mathbf{f}_t(s)$	$\in \mathbb{R}^3$ —Sum of all forces per unit s applied to the backbone by the tendons, in global frame coordinates.
$\mathbf{l}_t(s)$	$\in \mathbb{R}^3$ —Sum of all moments per unit s applied to the backbone by the tendons, in global frame coordinates.
$\mathbf{f}_i(s)$	$\in \mathbb{R}^3$ —Force per unit s applied to the i^{th} tendon by its surroundings.
$\mathbf{n}_i(s)$	$\in \mathbb{R}^3$ —Internal force in the i^{th} tendon.

τ_i $\in \mathbb{R}$ —Tension in the i^{th} tendon. It is constant along s under the frictionless assumption.

APPENDIX B

DERIVATION OF $f_i(s)$

Beginning with (11)

$$\mathbf{n}_i = \tau_i \frac{\dot{\mathbf{p}}_i}{\|\dot{\mathbf{p}}_i\|}$$

we rearrange and differentiate to obtain

$$\dot{\mathbf{p}}_i = \frac{1}{\tau_i} \|\dot{\mathbf{p}}_i\| \mathbf{n}_i, \quad \ddot{\mathbf{p}}_i = \frac{1}{\tau_i} \left(\frac{d}{ds} (\|\dot{\mathbf{p}}_i\|) \mathbf{n}_i + \|\dot{\mathbf{p}}_i\| \dot{\mathbf{n}}_i \right).$$

Noting that $\mathbf{n}_i \times \mathbf{n}_i = \mathbf{0}$, one can take a cross product of the two results above to find

$$\ddot{\mathbf{p}}_i \times \dot{\mathbf{p}}_i = \frac{\|\dot{\mathbf{p}}_i\|^2}{\tau_i^2} (\dot{\mathbf{n}}_i \times \mathbf{n}_i)$$

and therefore

$$\dot{\mathbf{p}}_i \times (\ddot{\mathbf{p}}_i \times \dot{\mathbf{p}}_i) = \frac{\|\dot{\mathbf{p}}_i\|^3}{\tau_i^3} (\mathbf{n}_i \times (\dot{\mathbf{n}}_i \times \mathbf{n}_i)).$$

Applying the vector triple product identity, $\mathbf{a} \times (\mathbf{b} \times \mathbf{c}) = \mathbf{b}(\mathbf{a} \cdot \mathbf{c}) - \mathbf{c}(\mathbf{a} \cdot \mathbf{b})$, we can expand the right-hand side of this equation. Since τ_i (the magnitude of \mathbf{n}_i) is constant with respect to s , then $\mathbf{n}_i \cdot \dot{\mathbf{n}}_i = \mathbf{0}$, and this results in

$$\mathbf{f}_i = -\dot{\mathbf{n}}_i = -\tau_i \frac{\dot{\mathbf{p}}_i \times (\ddot{\mathbf{p}}_i \times \dot{\mathbf{p}}_i)}{\|\dot{\mathbf{p}}_i\|^3}.$$

Using the fact that $\mathbf{a} \times \mathbf{b} = -\mathbf{b} \times \mathbf{a}$, and writing the cross products in a skew-symmetric matrix notation ($\mathbf{a} \times \mathbf{b} = \widehat{\mathbf{a}}\mathbf{b}$), we arrive at (12)

$$\mathbf{f}_i = \tau_i \frac{\dot{\mathbf{p}}_i \times (\dot{\mathbf{p}}_i \times \ddot{\mathbf{p}}_i)}{\|\dot{\mathbf{p}}_i\|^3} = \tau_i \frac{\widehat{\dot{\mathbf{p}}_i}^2}{\|\dot{\mathbf{p}}_i\|^3} \ddot{\mathbf{p}}_i.$$

REFERENCES

- [1] D. C. Rucker and R. J. Webster, III, “Exact mechanics of continuum robots with general tendon routing,” in *Proc. 12th Int. Symp. Exp. Robot. Springer Tracts Adv. Robot.*, 2010, to be published. Available: <http://iser2010.grasp.upenn.edu/?q=program>
- [2] G. Robinson and J. B. C. Davies, “Continuum robots—A state of the art,” in *Proc. IEEE Int. Conf. Robot. Autom.*, 1999, pp. 2849–2854.
- [3] S. Hirose, *Biologically Inspired Robots, Snake-Like Locomotors and Manipulators*. Oxford, U.K.: Oxford Univ. Press, 1993.
- [4] D. Trivedi, C. D. Rahn, W. M. Kierb, and I. D. Walker, “Soft robotics: Biological inspiration, state of the art, and future research,” *Appl. Bionics Biomech.*, vol. 5, no. 3, pp. 99–117, Sep. 2008.
- [5] R. J. Webster, III and B. A. Jones, “Design and kinematic modeling of constant curvature continuum robots: A review,” *Int. J. Robot. Res.*, vol. 29, pp. 1661–1683, 2010.
- [6] D. Trivedi, A. Lotfi, and C. Rahn, “Geometrically exact models for soft robotic manipulators,” *IEEE Trans. Robot.*, vol. 24, no. 5, pp. 773–780, Aug. 2008.
- [7] J. Wilson and U. Mahajan, “The mechanics of positioning highly flexible manipulator limbs,” *J. Mech., Transmiss., Autom. Design*, vol. 111, pp. 232–237, 1989.
- [8] K. Xu and N. Simaan, “Intrinsic wrench estimation and its performance index for multisegment continuum robots,” *IEEE Trans. Robot.*, vol. 26, no. 3, pp. 555–561, Jun. 2010.

- [9] K. Xu and N. Simaan, "Analytic formulation for kinematics, statics and shape restoration of multi-backbone continuum robots via elliptic integrals," *ASME J. Mech. Robot.*, vol. 2, no. 1, pp. 011 006–1–011 006–13, 2010.
- [10] D. C. Rucker, B. A. Jones, and R. J. Webster III, "A geometrically exact model for externally loaded concentric-tube continuum robots," *IEEE Trans. Robot.*, vol. 26, no. 5, pp. 769–780, Oct. 2010.
- [11] D. B. Camarillo, C. F. Milne, C. R. Carlson, M. R. Zinn, and J. K. Salisbury, "Mechanics modeling of tendon-driven continuum manipulators," *IEEE Trans. Robot.*, vol. 24, no. 6, pp. 1262–1273, Dec. 2008.
- [12] I. A. Gravagne, C. D. Rahn, and I. D. Walker, "Large-deflection dynamics and control for planar continuum robots," *IEEE/ASME Trans. Mechatron.*, vol. 8, pp. 299–307, Jun. 2003.
- [13] R. Buckingham and A. Graham. (2003). Reaching the unreachable—snake arm robots. in *Proc. Int. Symp. Robot.*, [Online]. Available: via OCRobotics Ltd. <http://www.ocrobotics.com>.
- [14] G. S. Chirikjian, "Hyper-redundant manipulator dynamics: A continuum approximation," *Adv. Robot.*, vol. 9, no. 3, pp. 217–243, 1995.
- [15] G. S. Chirikjian and J. W. Burdick, "Kinematically optimal hyper-redundant manipulator configurations," *IEEE Trans. Robot. Autom.*, vol. 11, no. 6, pp. 794–806, Dec. 1995.
- [16] G. S. Chirikjian and J. W. Burdick, "A modal approach to hyper-redundant manipulator kinematics," *IEEE Trans. Robot. Autom.*, vol. 10, no. 3, pp. 343–353, Jun. 1994.
- [17] C. Li and C. D. Rahn, "Design of continuous backbone, cable-driven robots," *ASME J. Mech. Design*, vol. 124, no. 2, pp. 265–271, 2002.
- [18] I. A. Gravagne, "Design, analysis and experimentation: The fundamentals of continuum robotic manipulators," Ph.D. dissertation, Dept. Elect. Comput. Eng., Clemson Univ., Clemson, SC, 2002.
- [19] I. A. Gravagne and I. D. Walker, "Manipulability, force, and compliance analysis for planar continuum robots," *IEEE Trans. Robot. Autom.*, vol. 18, no. 3, pp. 263–273, Jun. 2002.
- [20] J. H. Davis and R. M. Hirschorn, "A model for the embedded tendon control of a slender three-dimensional flexible robot link," *Dyn. Control*, vol. 4, no. 2, pp. 185–208, 1994.
- [21] B. Jones, R. Gray, and K. Turlapati, "Three-dimensional statics for continuum robotics," in *Proc. IEEE/RSJ Int. Conf. Intell. Robots Syst.*, 2009, pp. 2659–2664.
- [22] N. Simaan, J. Zhang, J. Roland Jr., and S. Manolidis, "Steerable continuum robot design for cochlear implant surgery," in *Proc. IEEE Int. Conf. Robot. Autom. Workshop*, 2010.
- [23] S. S. Antman, in *Nonlinear Problems of Elasticity*, S. Antman, J. Marsden, and L. Sirovich, Eds., 2nd ed. New York: Springer Science, 2005.
- [24] R. M. Murray, Z. Li, and S. S. Sastry, *A Mathematical Introduction to Robotic Manipulation*. Boca Raton, FL: CRC, 1994.
- [25] L. Shampine, "Solving hyperbolic P.D.E's in MATLAB," *Appl. Numer. Anal. Comput. Math.*, vol. 2, no. 3, pp. 346–358, 2005.
- [26] M. Bergou, M. Wardetzky, S. Robinson, B. Audoly, and E. Grinspun, "Discrete elastic rods," *ACM Trans. Graph.*, vol. 27, no. 3, 2008.



D. Caleb Rucker (S'07) received the B.S. degree in engineering mechanics and mathematics from Lipscomb University, Nashville, TN, in 2006. He is currently working toward the Ph.D. degree in mechanical engineering with Vanderbilt University, Nashville.

In 2007, he was an Engineer with Jacobs Technology Group, Tullahoma, TN. His current research interests include medical robotics, continuum robotics, mechanics-based modeling, control, and sensing.



Robert J. Webster, III (S'97–M'08) received the B.S. degree in electrical engineering from Clemson University, Clemson, SC, in 2002 and the M.S. and Ph.D. degrees in mechanical engineering from the Johns Hopkins University, Baltimore, MD, in 2004 and 2007, respectively.

In 2008, he joined the Faculty of Vanderbilt University, Nashville, TN, as an Assistant Professor of mechanical engineering, where he currently directs the Medical and Electromechanical Design Laboratory. His current research interests include medical

robotics, image-guided surgery, and continuum robotics.

Dr. Webster received the National Science Foundation CAREER Award in 2011.